Materials Science in Semiconductor Processing 168 (2023) 107842

Contents lists available at ScienceDirect

Materials Science in Semiconductor Processing

journal homepage: www.elsevier.com/locate/mssp

A DFT study of quantum electronic transport properties of InTeCl

Hira Batool [a], Abdul Majid [a,*], Mohammad Alkhedher [b], Niyazi Bulut [c], Ibrahim Al-Adwan [d]

[a] Department of Physics, University of Gujrat, Hafiz Hayat Campus, Gujrat, 50700, Pakistan
[b] Mechanical and Industrial Engineering Department, Abu Dhabi University, Abu Dhabi, United Arab Emirates
[c] Department of Physics, Faculty of Science, Firat University, Elazig, 23119, Turkey
[d] Department of Mechatronics Engineering, Faculty of Engineering Technology, Al-Balqa Applied University, 100190, Amman, Jordan

ARTICLE INFO

Keywords:
Density functional theory
InTeCl
NEGF
NEB
Transport properties

ABSTRACT

This work is carried out to investigate the structural, electronic and transport properties of InTeCl in bulk and slab periodicities using Density Functional Theory (DFT). The analysis of the structural parameters including bond length, lattice constants and bond angles of the materials was carried out in detail. The band gap of the material for the bulk and monolayer was found as 1.57 eV and 1.33 eV respectively. The direct to indirect transition of band gap is observed when the material is downscaled from bulk to the slab. Transport properties of the materials were computed using DFT based tight-binding method combined with non-equilibrium green functions (NEGF) formalism. The nano device Au–InTeCl–Au with fixed length of the central region was simulated to study IV-characteristics, transmission spectra and Hamiltonian states. Moreover, to check the diffusion properties of the material Nudged Elastic Band (NEB) calculations were carried out which revealed minimum transition barrier for bulk, slab and bilayer as 1.32 eV, 1.67 eV and 1.70 eV respectively. The current-voltage (IV) characteristic curves and transmission spectra for the materials were also studied to investigate the conductivity trend.

1. Introduction

During past few years, the formation of binary compounds having two different anions has gained a lot of research interest in order to design new compounds offering improved properties in comparison to the compounds with a single type of anions. To date, hundreds of binary compounds have been synthesized experimentally and predicted theoretically including sulfide silicates, oxychloride borates, oxide halides etc [1–10].

Metal chalcogenide halides (MCH) are ternary compounds, containing three different types of elements. These kinds of ternary compounds are synthesized by choosing different metals from the main and subgroups and then combing them with chalcogenides from oxygen to tellurium and halides from fluorine to iodine. The MCHs behave differently with individual anions while they exhibit completely different properties in the form of ternary compounds. In recent times, hundreds of MCHs have been investigated belonging to different classes of compounds including transition metal chalcogenides halides, rare earth metal chalcogenides halides. The major groups are further classified into sub-groups depending upon their properties, chemical composition and commonalities among them have been found at greater extent [3]. For example, niobium forms a large number of chalcogenide halide compounds with a different chemical composition of elements i.e. NbS_2Cl_2 [4], $Nb_2Te_2I_6$ [5]. However, group 8 elements (Mo, Cr and W) developed good chemistry with halide selenides, halide sulfides and halide oxides. The trivalent nature of chromium helps formation of MCH compounds like CrOBr [4,6], CrOCl [7] and CrSBr [8] that contain FeOCl-type structures [4]. Similarly, tungsten forms several halide oxides and halide sulfides which have been investigated for many potential applications. Hexavalent tungsten forms an isotopic series of MCH compounds in which different halogens and chalcogens crystallize in same symmetry by replacing each other. MCH have been studied at a larger scale for applications in the optics, thermoelectricity and electrochemistry. Due to their transportation properties, they are employed as solid-state electrolytes in batteries and as nonlinear optical materials.

Chalcogens and halogens have similar covalent radii but halogens are more electronegative which introduces diverse bonding. The addition of X (where X = F, Cl, Br, I) in chalcogenides results in increase of their optical band gap, by making their coordination polyhedra distorted while changes in densities are very small. These kinds of structural changes make metal chalcogenides halides a favorable candidate to fine-tune the structural and physical properties of halogens and halide-based

* Corresponding author.
E-mail address: abdulmajid40@uog.edu.pk (A. Majid).

https://doi.org/10.1016/j.mssp.2023.107842
Received 17 July 2023; Received in revised form 1 September 2023; Accepted 10 September 2023
Available online 14 September 2023

compounds [3]. Moreover, another polar compound BiTeI is important due to its spintronic character that helps introduce interesting effects including Rashba-type splitting [9] and pressure-induced topological phase [10,11]. The pressure-induced superconductivity in BiTeI and BiTeBr has been found [12]. The structural and electronic properties of AuTeI and PdTeI have been theoretically investigated [13]. The experimental results shows that InTeI undergoes phase transition as well as band gap transition from direct to indirect at about 15 GPa pressure [14]. The MCHs (M = Rh, Ga, C═Te, H═Cl) compounds have been predicted utilizing first-principles calculations and these compounds possess hole and electron mobilities up 4710 $cm^2V^{-1}s^{-1}$ and 1.5×10^4 $cm^2V^{-1}s^{-1}$ respectively [15,16]. These materials motivated researchers to explore more metal telluro-halide compounds for optoelectronic applications [13]. Metal telluro-halides have also been found attractive for applications in quantum computing due to the coexistence of topological states and superconductivity [17].

This work was carried out to theoretically investigate a moderate band gap semiconductor InTeCl belonging to space group $P2_1/c$ per crystal structure database [18] whereas it had been successfully synthesized in early 1980s [19,20]. Theoretically, 2D indium-based telluro-halides are predicted to be attractive materials owing to tunable electronic properties and anisotropic carrier mobility [21]. To our best knowledge, no data is present on structural, electronic and transport properties of InTeCl in bulk and slab periodicities. The present work is aimed at investigating and analyzing the structural, electronic and transport properties of bulk and 2D InTeCl using DFT based methodology. This investigation makes a substantial advancement in the field while also advancing our grasp of InTeCl's essential properties. The uniqueness of this research is found in the multidimensional analysis it employs to examine the properties of the material comprehensively. This study includes not only structural properties but also electronic and transport behaviour which will be helpful in realization of the material in nano electronic devices. This study opens the door to a better understanding of InTeCl's possible uses in electronic and optoelectronic applications by illuminating the intricate relationships between these features.

2. Computational details

The comprehensive investigation of the structural, electronic and transport properties of InTeCl in 2D and 3D were carried out using DFT. The linear combination of atomic orbitals (LCAO) technique implemented in BAND module of ADF (Amsterdam Density functional) package was used to perform the calculations [22]. The graphical user interface (GUI) of the code was used to set up the input files and parameters. BAND possesses the feature offering the choice of periodicity /dimensions (1D for chain, 2D for slab and 3D for bulk) to introduce the periodic boundary conditions on the structures. The monoclinic unit cell of InTeCl was taken as starting point and was simulated in bulk and slab periodicities to compute the properties of the material in 3D and 2D respectively.

Geometry optimization of the structures was performed without any constraints. The exchange correlation functional as Generalized Gradient Approximation with Perdew Burke Ernzerhof (GGA-PBE) was utilized for the calculations [23]. In the case of bilayer and 2D slab, GGA-PBE-D3 was also used to include Van der Waals (VdWs) interactions. The Slater type orbitals basis functions are implanted in ADF-BAND that are well-known for accurate prediction of electron interaction closer to the nucleus. In these calculations, we used TZP basis set with all electron calculations without freezing the core [24,25]. The relativistic effects become dominant with the increase in atomic number Z so relativistic effects within ZORA Hamiltonian were taken into account while performing these calculations [26]. The numerical integration was accomplished with convergence criteria of 1×10^{-6} eV. The structures were fully relaxed to get the geometrically optimized parameters during SCF cycles. The gradient convergence criterion was taken as 10^{-3} Hartree/Å for both periodicities and step convergence was 10^{-3} Hartree/Å for InTeCl bulk and 10^{-1} Hartree/Å for the slab. The entire calculations were ensured to be fully self-consistent. The electronic properties were studied by using different parameters. To calculate the electronic properties of optimized structures, single point (SP) calculations were carried out to calculate the nuclear gradients and derivatives of Hessian of the optimized geometry. The band structure of InTeCl (Bulk) was also calculated by using TB-mBJ functional as it is known to produce band structures comparable to experimental results [27,28].

To check the thermal stability we performed molecular dynamics (MD) simulations within the framework of the NVT ensemble with the time steps of 0.25 fs at temperature 300K. NHC (Nose Hoover Chain) thermostat was utilized to keep the temperature constant. The $2 \times 2 \times 2$ supercell of InTeCl was equilibrated for time 6 ps using 25000 steps.

The calculation of the electronic transport properties was performed using DFT and employing Non-Equilibrium Green Function (NEGF) approach. NEGF helps in the development of a quantitative quantum transport model. Poisson equation-based self-consistency via real space is utilized to treat the electrostatics. The expression of current (I) in the form of integral over voltage and energy-dependent magnitudes is given in equation (1) [29,30].

$$I = \frac{2e}{h} \int dE\, Tr\left\{\Gamma_L(E,V) G^r(E,V) \Gamma_R(E,V) G^a(E,V)\right\} \times f_L(E,V_b) - f_R(E,V_b) \ldots\ldots\ldots \quad (1)$$

Here G^a and G^r are retarded green functions and Γ is the spectral density of electrodes and f represents the Fermi-Dirac distribution of electrodes from left to right. The transmission function is represented as given in equation (2),

$$\overline{T}(E,V_b) = Trace\left[\Gamma_L V_b\, G^R(E,V_b) \Gamma_R V_b\, G^A(E,V_b)\right] \quad (2)$$

The equilibrium conductance for two terminal devices calculated utilizing transmission coefficients is given in equation (3),

$$G = \frac{2e^2}{h}\, \mathrm{T}\left(\mathrm{E_f}, \mathrm{V_b} = 0\mathrm{V}\right) \quad (3)$$

DFTB module was used to model Hamiltonian and overlap matrices of electrode/channel regions and to compute the Fermi energies at equilibrium. In this approach, periodic boundary conditions within Γ point approximation are utilized to represent crystals for transport calculations [31,32].

The variation in coupling surface distances for Au–In, Au–Te, and Au–Cl was set in range from 1.5 Å to 3.5 Å with step size of 0.3 Å, that was chosen on the basis of following considerations; (i) The chosen range of coupling distances encompasses a spectrum of interaction regimes, from short to long distances. (ii) The simulations ensure numerical convergence while capturing the coupling effects accurately. The choice of extremely short distances may lead to rapid convergence issues due to high interaction strengths, while excessively long distances can result in negligible coupling. Hence, the selected range strikes a balance to mitigate these challenges.

The nudged elastic band (NEB) method was employed to investigate the transition states in slab, bulk and bilayer forms of InTeCl along different sites. This method involves dividing the reaction pathway into a series of discrete intermediates and then optimizing the geometry of each considered image using a combination of energy minimization and constrained dynamics [33,34]. In the NEB method, a path along with starting and terminal states as well as a series of intermediate structures, or "images", are placed along this path. The energy of each image is minimized subject to a set of constraints that ensure that the path remains continuous and that the images remain evenly spaced. The energy barrier for the reaction is then calculated as the difference between the highest-energy image and the lowest-energy image. The method can provide detailed insights into the mechanisms of chemical reactions and

can help guide the design of new catalysts and materials [35,36]. The total force on the ith image is given using equation (4).

$$F_i = |F_i{}^S|_{\parallel} - |\nabla E(R_i)|_{\perp} \ldots \ldots \quad (4)$$

Where F_i is the summation of all forces on the considered image, $|F_i{}^S|_{||}$ represents spring restoring force and $|\nabla E(R_i)|_{\perp}$ shows true force. The maximum value of the energy of the considered image is calculated by equation (5).

$$F_{i\ max} = \nabla E(R_{i\ max}) + 2\nabla E|R_{i\ max}|_{\parallel} \ldots \ldots \quad (5)$$

In the calculations, three paths are taken into account: the first one is for InTeCl slab along Y-axis, the second is for InTeCl bulk along the y-axis and the last one is for InTeCl along the y-axis.

3. Results and discussion

The geometry of the materials was fully relaxed to obtained optimized structure prior to computing the structural, electronic and transport properties. The computed results and discussion on the findings to exhibit the properties of the materials are described below.

3.1. Structural properties

The structural properties of a material determined upon full relaxation are examined by analyzing the lattice parameters including bond lengths, lattice constants and angles. InTeCl belongs to the chalcogenide halides of group IIIA having the general formula MYX (M = B, Al, In, Ti; X = S, Se, Te and Y=I, Br, Cl). The complete series of its chalcogenides halides compounds for indium are known out of which InTeCl is found to be more stable and appeared in form of monoclinic structure with space group $P2_1/c$. The electronic configuration for In, Te and Cl is [[Kr], $4d^{10}$, $5s^2$, $5p^1$], [[Kr], $4d^{10}$, $5s^2$, $5p^4$] and [[Ne], $3s^2$, $3p^5$] respectively. The coordination number for Te is found to be 4 only due to the greater covalency of In–Te bonding and the size of Te atom. The structure of InTeCl is found in such a way that the edges of the tetrahedron are occupied by Te atoms and the coordination number for chlorine is one for each tetrahedron and Cl does not show significant probability to produce layered structure [37]. In a layer, three Te atoms and one Cl atom surround In atoms, as shown in Fig. 1. The neighboring tetrahedrons share the connecting Te–Te edges to form dimeric units of tetrahedron while Cl atoms are occupied by trans-terminal positions [20,38,39]. There are two nonequivalent In^{3+} sites. In the first In^{3+} site, In^{3+} is bonded to three Te^{2-} and one Cl^{1-} atom to form distorted edge-sharing InTeCl tetrahedra. There is a spread of In–Te bond distances ranging from 2.83–2.89 Å. The In–Cl bond length is 2.44 Å. In the second In^{3+}site, In^{3+} is bonded in a 5-coordinate geometry to three Te^{2-} and two equivalent Cl^{1-} atoms. There is a spread of In–Te bond distances ranging from 2.83–2.94 Å. There is one shorter (2.43 Å) and one longer (3.95 Å) In–Cl bond length. There are two nonequivalent Te^{2-} sites. In the first Te^{2-} site; Te^{2-} is bonded in a 3-coordinate geometry to three In^{3+} atoms. In the second Te^{2-} site; Te^{2-} is bonded in a 4-coordinate geometry to three In^{3+} and one Cl^{1-} atom. The Te–Cl bond length is 3.70 Å. There are two nonequivalent Cl^{1-} sites. In the first Cl^{1-} site, Cl^{1-} is bonded in a distorted single-bond geometry to two equivalent In^{3+} atoms. In the second Cl^{1-} site, Cl^{1-} is bonded in a distorted single-bond geometry to one In^{3+} and one Te^{2-} atom. The lattice constants are a = 14.38 Å, b = 7.34 Å and c = 7.77 Å which agree well with the reported values a = 7.20 Å, b = 14.29 Å and c = 7.61 Å [19]. The average inter-atomic distance between In–Te (2.85 Å), In–Te (2.84 Å), In–Te (2.90 Å), In–Te (2.93 Å) and for Cl–In (2.44 Å) Cl–Te (3.95 Å) and the value of α = 87.19° and all these calculated values accord with the relevant literature [19,40].

The optimized structure of 2D slab of InTeCl having 22 atoms is depicted in Fig. 2. The lattice constants are a = 7.20 Å and b = 14.29 Å with $\alpha = \beta = \gamma = 90^{\circ}$ which shows that 2D InTeCl follows rectangular crystal structure with glide plane symmetry. The average interatomic distances for 2D InTeCl are In–Te (2.86 Å), Te–In (2.75 Å), Cl–In (2.38 Å), and In–Cl (2.61 Å). The bond lengths in 2D are shorter in range as compared to the bulk InTeCl indicating that 2D layers have tendency to come closer to achieve local minima and maximum overlap of the orbitals [41].

The geometry optimization of two formula units of InTeCl was carried out to obtain a bilayer by keeping them apart at a distance of 2.34 Å with both in-plane and out-of-plane anisotropy to check the possibility of layeredness in InTeCl. The in-plane anisotropy is found more stable than the out-of-plane anisotropy of the InTeCl bilayer.

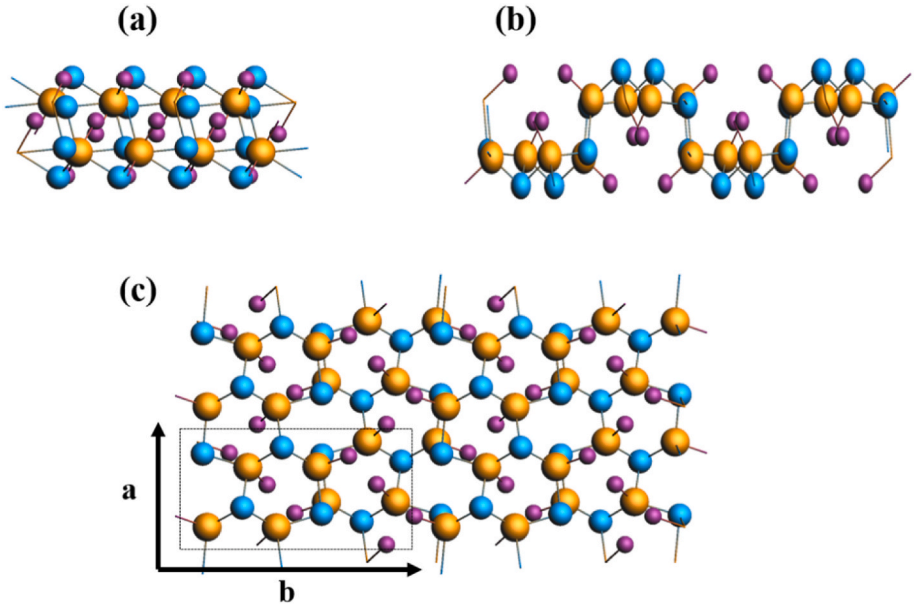

Fig. 1. The optimized structure of bulk InTeCl. (a) Viewed along the x-axis, (b) viewed y-axis, (c) viewed along z-axis. The unit cell is marked as squared box. Here orange, blue and purple colored spheres are representing indium, tellurium and chlorine atoms respectively.

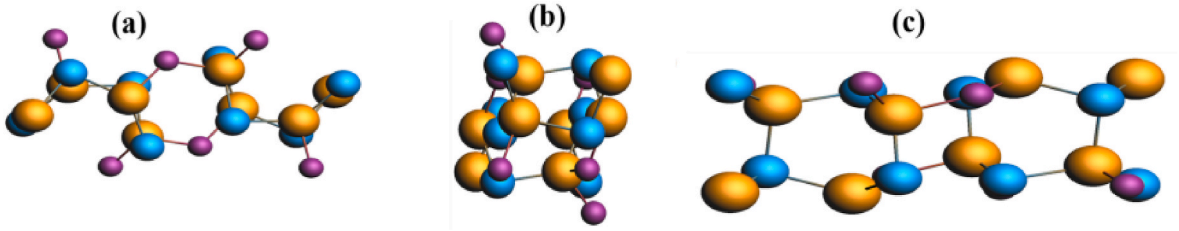

Fig. 2. The optimized structure of InTeCl slab (a) viewed along the x-axis, (b) viewed y-axis, (c) viewed along z-axis.

3.2. Charge analysis

3.2.1. Electron localization function (ELF)

To study electron localization in solids, the ELF helps to understand the bonding and formation of compounds [42]. The values of the ELF function lie in the range of 0–1 which indicates electron delocalization and electron localization respectively whereas an ELF value of 0.5 corresponds to the equal distribution of localized and delocalized electronic densities in the material [43]. As shown in Fig. 3(a) there are two electron localization regions in InTeCl bulk, one around Te and the other around Cl atoms while the ELF value for In is 0.5 which indicates equal distribution of electron densities. It points to covalent bonding between In–Te and In–Cl bonds. Therefore, the electronegativity differences between the In–Te and In–Cl bonds calculated from the Pauling scale are 0.32 and 1.38 which also supported the covalent characteristics of these bonds [44]. The ELF plot for InTeCl slab is shown in Fig. 4(a) where there is no charge density near 0 ELF value and there are well-defined localization regions around Te and Cl atoms. While In has equally localized and delocalized densities and charge densities as in bulk which represents polar covalent characteristics between In–Te and In–Cl bonds.

3.2.2. Hirshfeld charges

Hirshfeld charge analysis was carried out to examine the charge transfer between In, Te and Cl atoms in bulk InTeCl [45]. The computed values of charges (in units e) are In(1) = In(2) = In(3) = In(4) = 0.231, In(5) = In(6), In(7) = In(8) = 0.234, Te(1) = Te(2) = Te(3) = Te(4) = −0.006, Te(5) = Te(6) = Te(7) = Te(8) = −0.18, Cl(1) = Cl(2) = Cl(3) = Cl(4) = −0.204, Cl(6) = Cl(7) = Cl(8) = −0.238. The overall values of Hirshfeld charges on In, Te, and Cl in bulk InTeCl are 1.904 e, −0.076 e and −1.824 e respectively. Here, In carries a positive charge while Cl and Te carry negative charges to transfer charge from In to Cl and Te upon bond formation in bulk InTeCl. The Hirshfeld analysis of bulk InTeCl is shown in Fig. 3(b) where blue (red) color on the scale represents positive (negative) charge. In atoms at the edges carry less charge and transfer maximum charge to Cl atoms only while the central atoms carry more charge and transfer charge to both Cl and Te atoms. Similarly, the Hirshfeld analysis for InTeCl slab is shown in Fig. 4(b). The overall behavior of charge transfer is same as in bulk compound i.e. more charge is transferred from In at edges to Cl atoms while central In atoms transfer charge to both Te and Cl atoms.

3.2.3. Electronegativity consideration

The electronegativity differences between In–Te, In–Cl and In–Te are 0.32, 1.38 and 1.06 respectively which suggest polar covalent bonding. The bonding character is usually determined utilizing ionic, covalent and van der Waal radii. The covalent radii of In, Te and Cl are 1.42 Å, 1.38 Å and 1.02 Å and the sum of covalent radii of In–Te, In–Cl and Te–Cl are 2.74 Å, 2.44 Å and 2.4 Å [46]. Similarly, the ionic radii of In, Te and Cl are 0.94 Å, 2.07 Å and 1.81 Å and the sum of ionic radii in In–Te, In–Cl and Te–Cl are 3.01 Å, 2.75 Å and 3.88 Å respectively [47]. The computed bond lengths of In–Te (2.85–2.93 Å), Cl–In (2.44 Å) and Cl–Te (3.95 Å) in bulk showing that the sum of covalent radii is smaller than computed bond lengths while the sum of ionic radii is greater than the computed bond lengths which clearly exhibits the covalent character. Similarly, the bond lengths in In–Te (2.86 Å), Te–In (2.75 Å), Cl–In (2.38 Å), and In–Cl (2.61 Å) in slab that shows that the sum of covalent radii is smaller than the computed bond lengths in case In–Te and for In–Cl bonds in the center of layer while In–Cl at edges shows opposite behavior showing its tendency to become ionic in case of the slab due to redistribution of charge in 2D periodicity.

The electronegativity of InTeCl compound is calculated by the formula [48] given in equation (6).

$$\mathscr{X} = \left[x\,(A)^{a} x(B)^{b} x(C)^{c}\right]^{1/a+b+c} \tag{6}$$

Here, $\mathscr{X}$ represents electronegativity whereas a, b and c are the number of atoms in a compound. The calculated electronegativity of InTeCl compound is 2.28 which is greater than 1.7 depicting that it has a dominant ionic character as a whole. The percentage ionic character is determined by the Pauling formula given in equation (7).

$$\%\ \text{Percentage ionic character} = \frac{\Delta E}{1.7}\ \text{x}\ 50 \tag{7}$$

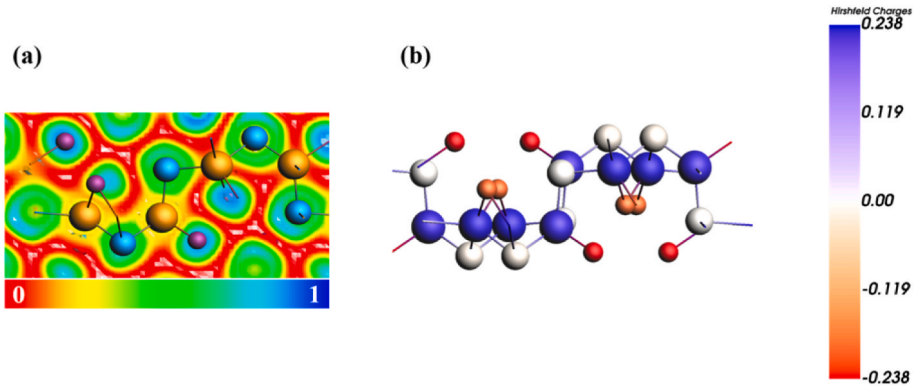

Fig. 3. The charge analysis of InTeCl bulk (a) Plot of electron localization function in which red color represents low charge density while blue color is associated with electron localization. (b) Hirshfeld charge analysis where blue (red) color represents positive (negative) charge.

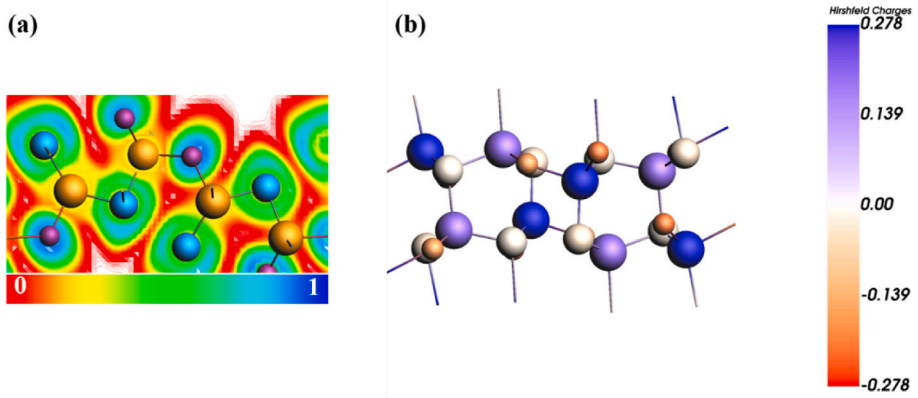

Fig. 4. The charge analysis of InTeCl slab (a) Plot of the Electron Localization Function (b) Hirshfeld charge analysis in which blue color represents positive charge and red color represents negative charge.

The percentage ionic character is 67% hence InTeCl bulk has a dominant ionic character that agrees with ELF analysis in Fig. 3.

3.2.4. Stability

The structural, dynamical and thermal stability of the materials are determined on the basis of calculated findings. To analyse the structural stability of InTeCl in bulk and slab, the formation energy is calculated which is defined in equation (8),

$$E_{form=}\frac{xE_{In} - yE_{Te} - zE_{cl} - E_{InTeCl}}{x+y+z} \quad (8)$$

$E_{In}, E_{Te}, E_{Cl,}$ *and* E_{InTeCl} are respective total energies of In, Te, Cl atoms and InTeCl compound whereas x, y and z are the total number of atoms in a unit cell [49]. The entire materials studied herein correspond to the exothermic reactions with the value of the formation energy for InTeCl bulk as 0.95 eV and for InTeCl slab as 0.84 eV per formula unit. The phonon dispersion helps to explore the dynamic stability of a compound. The computed phonon band structure of InTeCl in bulk and slab are shown in Fig. 5 (a) & (b) respectively. The analysis indicates the absence of soft phonon modes in the entire Brillouin zone which show that both bulk and 2D InTeCl are kinetically stable.

In order to achieve true stability of the materials, both phonon and MD simulations were performed with 2 × 2 × 2 large super cells. The molecular dynamics simulations were performed at 300 K with the time evolution of 6 ps. There was no deformation and bond breakage in structure which indicates that InTeCl possess good thermal stability as well. In Fig. 6 (a) & (b), the temperature and energy are plotted with the mentioned time steps and Fig. 7 which displays the snapshots obtained after time steps of 6 ps. The data indicates that after 2 ps the structure's overall energy almost stays constant. It is thus concluded that structure of InTeCl in bulk is well-maintained at 300 K which points to the material's thermal stability at room temperature.

3.3. Electronic properties

The electronic properties of the materials were examined to check the conductivity and electronic transport character for applications in nanoscale electronic devices. In what follows, the electronic properties of InTeCl bulk, slab and bilayer are described. Figs. 8 and 9 depict the band diagram and total density of states (DOS) of InTeCl bulk which reveals its direct band gap semi-conductor nature with the band gap value of 1.57 eV which is larger than reported band gap of InTeI (i.e. 1.29 eV) [14].

As PBE functional underestimate band gaps, the band gap was also

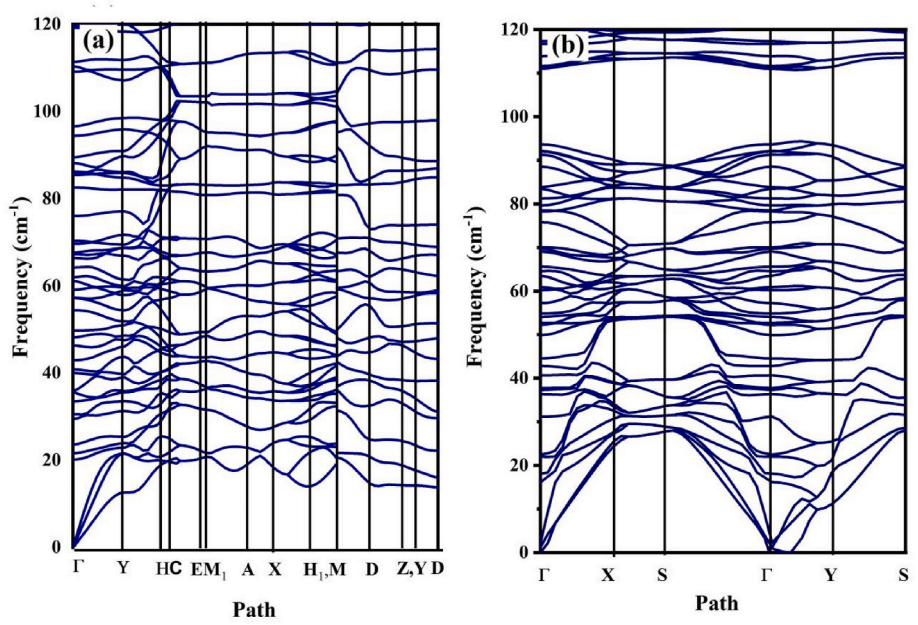

Fig. 5. The calculated Phonon Band structure of (a) InTeCl Bulk (b) InTeCl Slab.

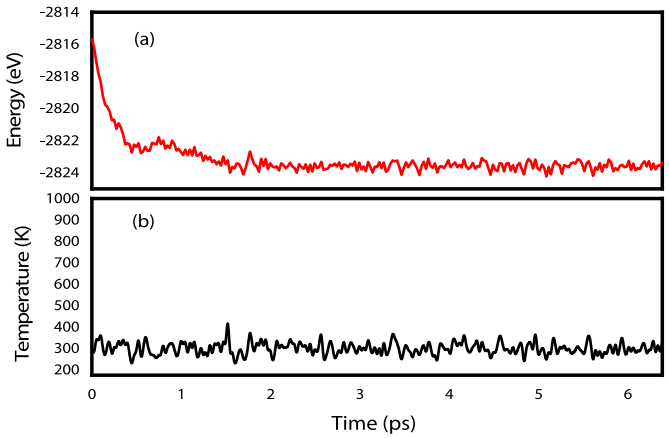

Fig. 6. The changes in temperature and unrestricted energy of the super cell of the InTeCl (Bulk) as a function of time as determined from MD simulations.

calculated by TB-mBJ level of theory which is known to provide accurate electron correlational energies in several solids. The TB-mBJ calculated band diagram of InTeCl bulk is shown in Fig. 9(b) that exhibits band gap of 2.56 eV. InTeCl has a direct band gap as Conduction Band Minima (CBM) and Valence Band maxima (VBM) lie at the Γ point. The calculated total and partial density of states (PDOS) of InTeCl are shown in Fig. 8 (a) & (b), according to which Te and Cl show major contribution in VB due to Te-p and Cl-p orbitals while in the CB, the major contribution emerges from In-p orbitals with a small contribution of In-s orbitals.

The analysis of PDOS reveals hybridization between states of In, Te and Cl atoms due to strong interaction between In-p, In-s, Cl-p and Te-p orbitals as shown in Fig. 8(b). It is found that p-states are found in the majority at band edges and these play major role in determining the electronic conductivity of InTeCl. The band structure of 2D InTeCl also revealed a semiconductor nature with an indirect gap of 1.33 eV. It means that there is a direct to indirect transition of band gap when the material is downscaled from bulk to the slab. The total and partial DOS are also calculated for the 2D slab which revealed a major contribution of Te and Cl relate states in the VB and In related states in the CB.

A major contribution of Te-p and Cl-p in the VB and a significant contribution of In-s orbitals is observed in the CB near the Fermi level as shown in Fig. 11. The top of the VB is located at X-point and VB is found closer to the Fermi level (E_F) as plotted in Fig. 10 (b). The band structure of InTeCl bilayer also shows its semiconducting nature with the indirect band gap of 0.56 eV, per Fig. 10 (a), satisfying the fact that an increase in thickness or the number of layers decreases the band gap. The band gap of bilayer is comparable to germanium making it a promising candidate for many potential applications.

3.4. Electronic transport properties

The calculated electronic transport properties of the materials are described in this section. The transport properties of 2D InTeCl were investigated using NEGF methodology. The flow of tunneling current could be simulated over the state of open boundaries and non-equilibrium states between the two contacts. We successfully implemented NEGF to investigate the transport properties of the mentioned material in line with the established methodology [50]. By keeping in mind the usage in transistors, the external field was applied along the z-direction i.e. perpendicular to the surface of the material and thus we attempted to study the IV characteristics and mobility of electrons [51].

The system under consideration is two probe device comprised of left electrode, the central region and the right electrode [52]. The central region contains InTeCl in Bulk and slab form with different lengths along with an electrode extension to make sure a smooth conduction between the electrodes and central region potential. The device named as Au–InTeCl–Au is shown in Fig. 12 and length of the central region is labeled by the number of InTeCl unit cells (UC) [53]. The distance between electrodes and the central region was fixed for all Au–InTeCl–Au

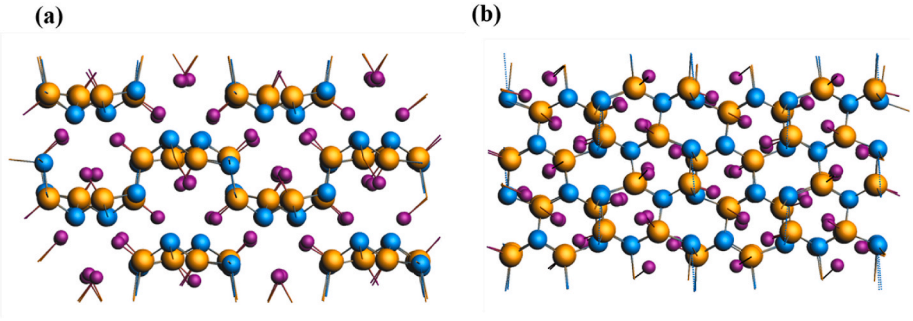

Fig. 7. Snapshots of structural changes in the super cell of the InTeCl (Bulk) after 6 ps (a) along y –axis (b) along z-axis.

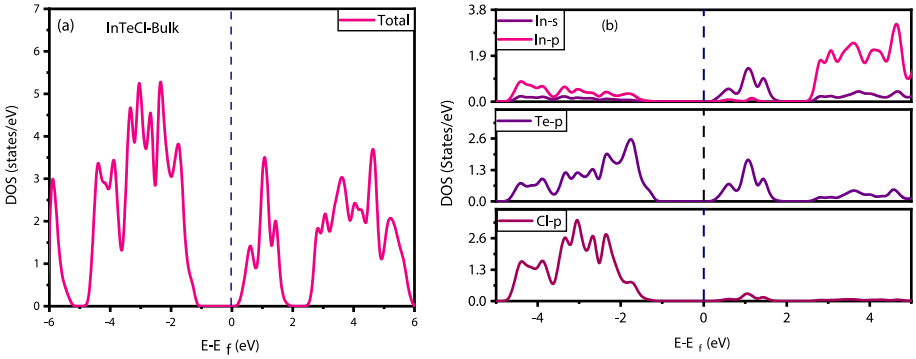

Fig. 8. (a) Total electronic density of states (DOS) computed for InTeCl in bulk and (b) PDOS of InTeCl in bulk. Fermi level is shifted to 0 eV and is shown by red vertical line.

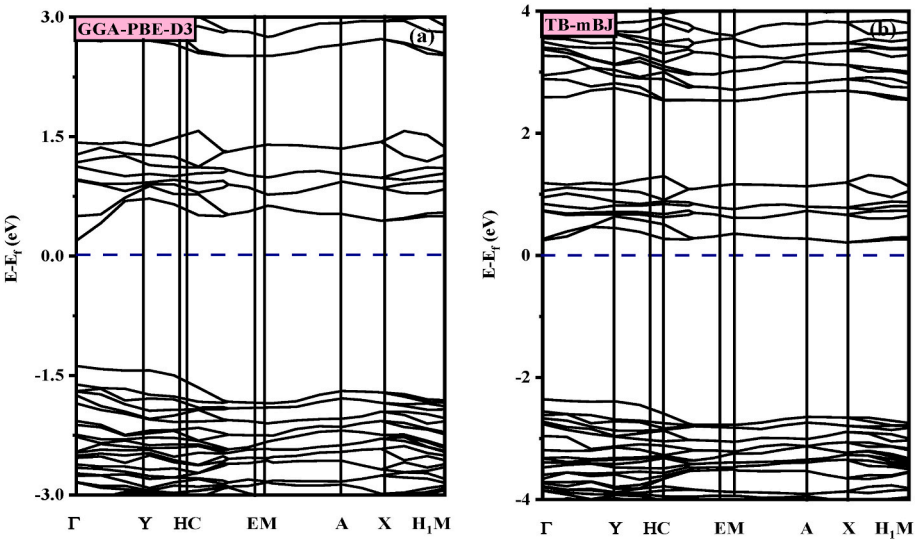

Fig. 9. The band structure of InTeCl (Bulk) calculated using (a) GGA-PBE-D3 (b) TB-mBJ. Fermi level is shifted to 0 eV and is shown by horizontal line.

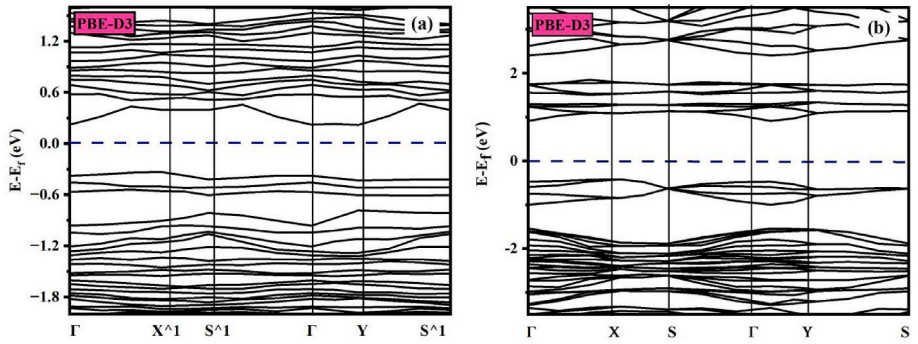

Fig. 10. The band diagram calculated for InTeCl in (a) Bilayer (b) Slab. The position of Fermi level is shifted to 0 eV and is shown by horizontal line.

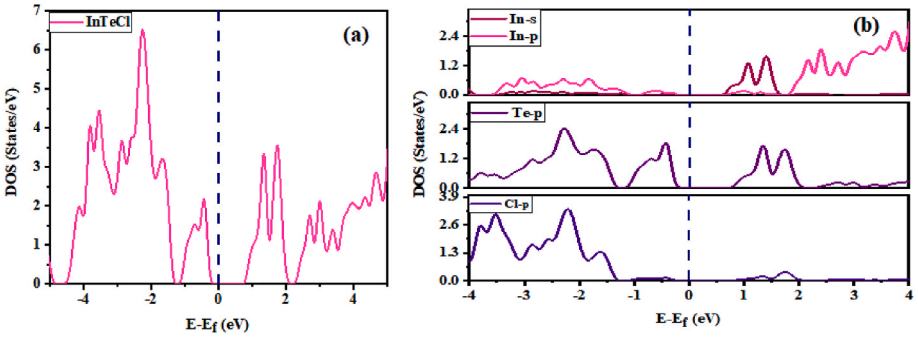

Fig. 11. (a) Total DOS of InTeCl slab (b) PDOS of InTeCl slab. The position of Fermi level is shifted to 0 eV and is shown by vertical line.

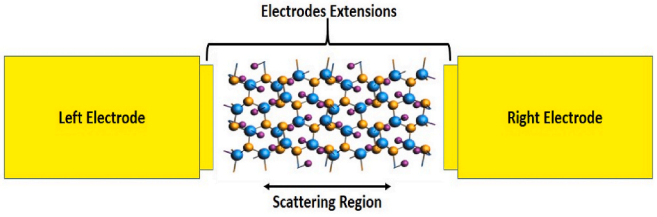

Fig. 12. Schematic diagram of two-probe nano device. The yellow color is representing Gold electrodes whereas the scattering region comprised of InTeCl compound.

devices. The left and right electrodes directly couple the In, Te and Cl atoms and the coupling distance between respective atoms as Au–In, Au–Te and Au–Cl were 2.89 Å, 3.11 Å and 2.46 Å respectively at right electrode. On the other hand, at left electrode the coupling distances between Au–In, Au–Te and Au–Cl were 2.6 Å, 1.67 Å and 2.34 Å respectively. The binding energy formula was used to determine the values of coupling distance between electrodes as per equation (9),

$$E_{Binding} = E_{Total}[InTeCl + Au] - E_{Total}[InTeCl] - E_{Total}[Au] \quad (9)$$

The coupling surfaces distance of Au–In, Au–Te and Au–Cl varied from 1.5 Å - 3.5 Å with a minimum step rate of 0.3 Å. Then we determined the value of coupling surface distance using principle of energy

minimization. The method was adopted to determine the coupling distance of electrodes in nanodevices including zinc oxide (ZnO) nano-rods [54], ZnO nanotubes [55] and boron nitride nanotubes [56,57]. The channel lengths bulk-UC, bulk-2x2, slab-UC and slab-2x2 are 1.5 nm, 2.9 nm 1.15 nm and 2.7 nm respectively.

First, the transport properties of n-InTeCl nanodevices at equilibrium will be described. The transmission spectra of InTeCl in bulk UC and 2 × 2 supercell (SC) and 2D UC and 2 × 2 SC by varying the channel lengths at 0 V are shown in Fig. 13. It can be observed that there are multiple peaks in the energy range and these peaks are associated with the existence of multiple transmission channels in that region. Near the E_F, transmission spectrum showed different behavior, transmission is about zero, as per Fig. 13 (d), around the E_F but non-zero in Fig. 13 (a), (b) & (c). This phenomena could be explained with the fact that there is direct tunneling from one electrode to other that caused transmission near the E_F. The existence of broad resonance around the E_F is distinctive feature of these transmission spectra, given particularly in Fig. 14 (a) & (b). The strong transmission spectra should possess two features [58], (i) It should have broad resonances so that the current induced effects of interface geometry could be reduced. (ii) It should have larger transmission probability around the Fermi energy of electrode to create a good conduction from nanowire junctions.

To check the effects of the interface between Au electrodes and InTeCl the DOS of n-InTeCl nanodevices including Au atoms and PDOS of InTeCl without Au atoms are calculated at equilibrium [59]. Fig. 15 shows that the shapes of DOS for Au–InTeCl nanodevices are the same as PDOS of InTeCl. However, near the E_F peaks in the DOS are higher due to the interfaces states which means that these states are responsible for transmission spectrum around the E_F [60]. For n-Au-InTeCl nanodevices, the interface states seem to overlap each other, and create a transmission channel near the Fermi level.

Transmission Eigen State (TES) values near the E_F were also calculated and shown in Fig. 14. The TES are a group of eigen states in the NEGF approach which explain the system's transport characteristics [61]. The coherent electronic transport modes via a scattering region linked to two or more leads are represented by these eigen states [62]. TES exhibit larger amplitude at the center of the scattering region as shown in Fig. 14(a). The TES on the leftmost side represents both reflective and incident states and hence these both states interfere constructively or destructively. The amplitude of the eigen states around indium atoms is almost zero confirming destructive interference whereas in the region around Te and Cl atoms the eigen states are interfering constructively, as shown in Fig. 14 (a). Similarly, Fig. 14 (b) shows the maximum amplitude of TES at right which means most of the eigen states are transmitted. These results showed that there is a gradual change in TES from localized to delocalized states in the channel/scattering region towards one electrode by increasing channel length [62,63].

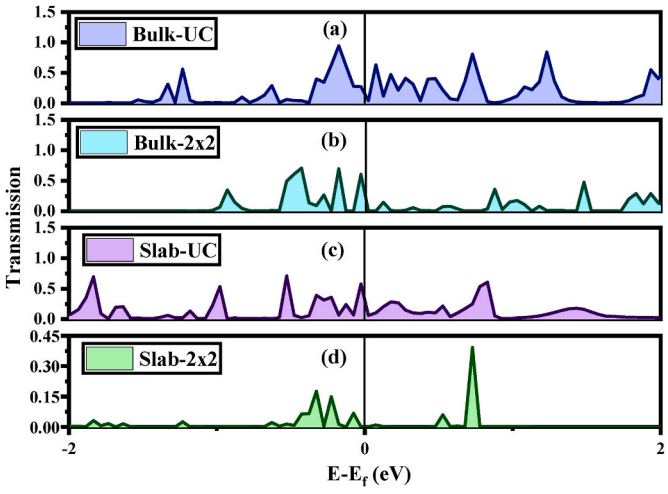

Fig. 13. The calculated transmission spectra of n-InTeCl nano devices at 0 V. (a) n = 1 for bulk, (b) n = 2 for bulk, (c) n = 1 for slab, (d) n = 2 for slab. The E_F is set to zero and is represented by vertical line.

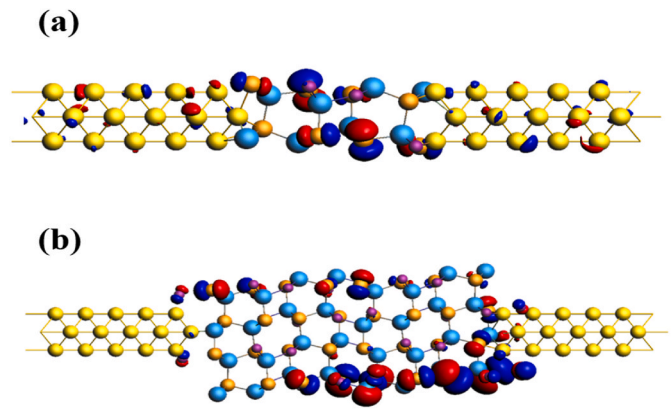

Fig. 14. The calculated transmission eigenstates for n-InTeCl slab based devices at E_F.

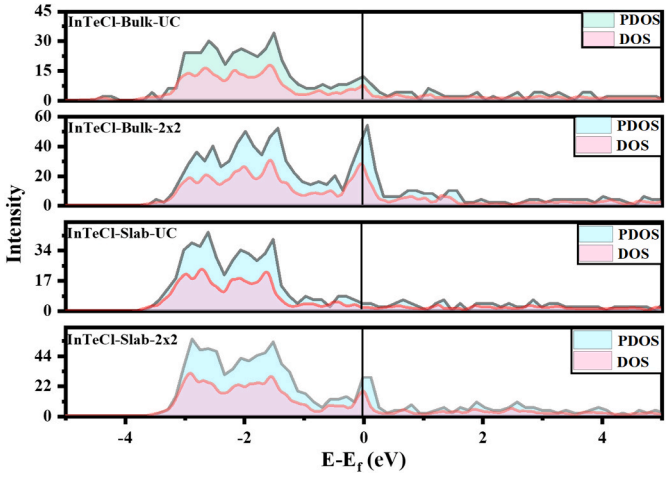

Fig. 15. The calculated Density of states for the scattering region of the nanodevices and Projected density of states for InTeCl nanodevices including Au electrodes at equilibrium whereas E_F is set to zero.

Besides the transmission spectra that are not quite sufficient to describe transport properties at equilibrium, we calculated the current-Voltage (IV) characteristic curve for n-Au-InTeCl nanodevices as shown in Fig. 16. There is strong nonlinear behavior in the nanodevices which seem to possess Schottky-type electronic structure. In the same biasing range i.e. −3 V–3 V, the value of current was decreased by increasing channel length. There IV curve was linear in the regions (−0.24 V, 0.24 V), (−0.4 V, 0.4 V), (−0.4 V, 0.4 V), (−0.56 V, 0.5 6 V) for bulk-UC, bulk-2x2, slab-UC, slab-2x2 respectively and showed metallic behavior. The current increased linearly at first but later it increased exponentially as in Schottky-diodes which is consistent with the fact that current is driven by the electrochemical potential in ballistic conductors which is why it goes up at first and then drops and so on [64]. The InTeCl-bulk exhibits better rectification characteristics in n-InTeCl nanodevices.

To understand the rectification characteristics the transmission spectra of n-InTeCl bulk (n = 1, 2) were calculated under different biasing voltages. The total current is contributed by electronic states present in biasing window [$\mu_L(V_b)$, $\mu_R(V_b)$] region. Here, the E_F, the chemical potential of the left electrode μ_L and right electrode μ_R are set to zero [65]. In order to explain the variation in current, Fig. 17 shows

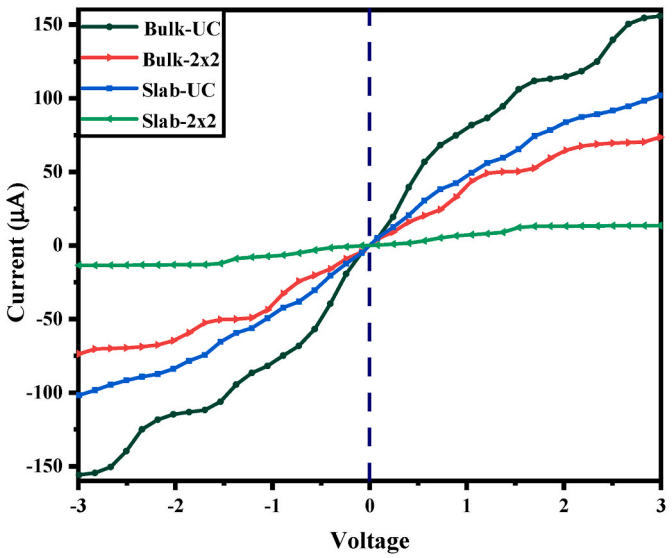

Fig. 16. The NEGF Current-Voltage curves calculated for n-Au-InTeCl nano-devices. UC means unit cell whereas 2 × 2 referes to supercell.

the NEGF transmission spectrum calculated for Au–InTeCl bulk unitcell (a-e panels) and Au–InTeCl bulk-2x2 supercell (f-j panels). In case of the device containing unitcell, a small transmission peak detected in the biasing window −0.2 V–0.2 V (panel a) which explains small current in the start. Later, with increase in the biasing voltage, more transmission peaks occurred in the biasing window (panels b to e) which indicates an increase in the current. In case of the device containing supercell, few transmission peaks appear in the window (panel g) pointing to small current in the start. Later, more transmission peaks appeared in the biasing window (panels g to j) that indicates a linear increase in the current. In contrast to the supercell based device (panels f to j), more and higher transmission peaks appeared outside the window in case of unitcell based device (panels a to f) which is reason behind comparatively higher currents in it.

The spatial distribution of the frontier molecular orbitals can also be used to examine the characteristics of electron transport. The highest occupied molecular orbital (HUMO) is the one that corresponds to the first transmission peak below the E_F. The lowest unoccupied molecular orbital (LUMO) corresponds to the first transmission peak above the E_F. The molecular-projected self-consistent Hamiltonian (MPSH) offers rectification properties in the form of HOMO and LUMO. The transmission peak, which is connected to the poles of the Green's function, is determined by the MPSH eigenstates [58]. These are relevant to the bias window of the transmission spectra [65]. The HUMO and LUMO calculated for 2-Au-InTeCl bulk device show four MPSH states as given in Fig. 18. The transmission peaks given in Fig. 18 correspond to these MPSH states showing notable densities around atoms. At biasing voltages 0.8 V and 1.2 V, the orbitals were delocalized and offered no difficulty in the formation of the transmission channel that resulted in large circuit in these devices.

As electrons flow from the electrodes into the central region, their densities redistribute around the nuclei. This redistribution affects the local electronic structure, altering energy levels and creating energy-dependent transmission probabilities. Transmission peaks in the spectra correspond to energy levels where resonance occurs. The coupling of electronic states causes electrons to be efficiently transmitted through the central region. These peaks are influenced by the arrangement of atoms, their electronic orbitals, and the modulation of electron densities due to the presence of the central region. The energy levels of the central region orbitals may align with those of the electrode orbitals, leading to enhanced electron tunneling. The MPSH captures these interactions, and the transmission spectra reveal the energy levels at which these hybridization effects lead to transmission peaks.

3.5. Diffusion path study

The energy barrier in nudged elastic band (NEB) simulation helps finding the energy to overcome the transition state between the reactants and products. This energy barrier can be calculated from the energy profile obtained from the NEB simulation and is typically reported as the maximum energy along the reaction path. The value of the energy barrier is an important property that determines the rate of a reaction or process. The results with minimum transition barrier energies are studied here [66].

To shed light on the diffusion properties of InTeCl the investigation of the migration pathways is crucial. InTeCl offers the transition energy barrier during the diffusion of an external atom which has to be measured. CI-NEB simulations were performed to find energy barriers faced by Li in InTeCl slab, bulk and bilayer with energy calculated for different images as shown in Fig. 19. The transition pathway for 2D InTeCl slab shown in Fig. 19 (a) points out the minimum energy barrier

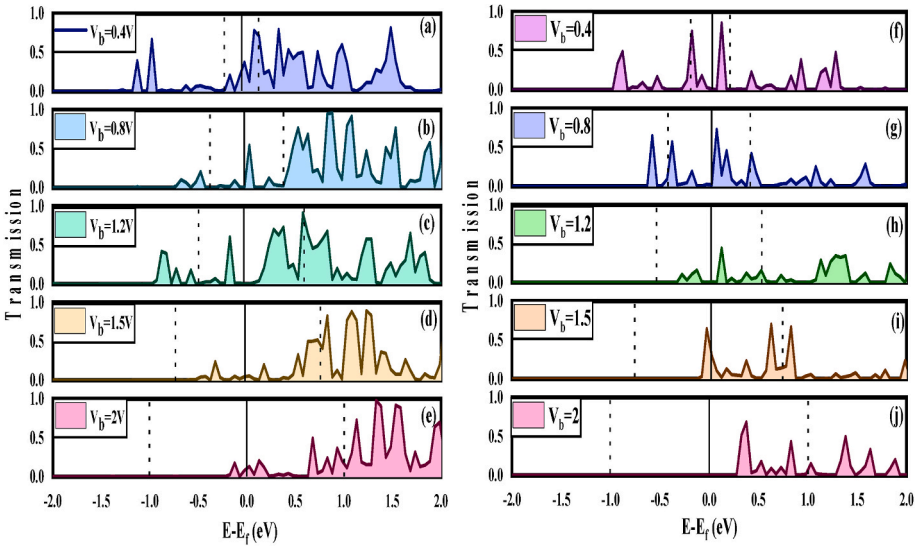

Fig. 17. The NEGF transmission spectrum calculated for Au–InTeCl-Bulk-UC (a–e) and Au–InTeCl-Bulk-2x2 (f–j). A biasing window is represented by dotted lines and the E_F is set to zero.

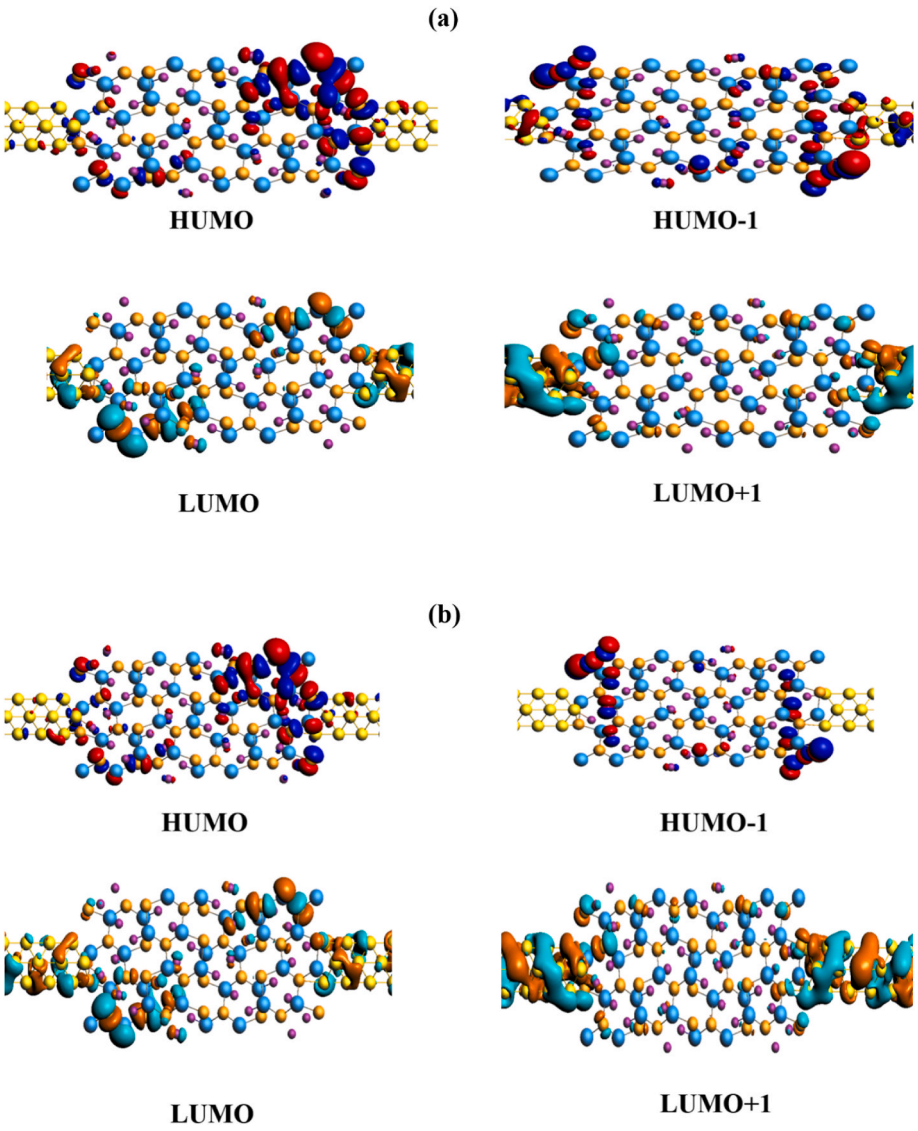

Fig. 18. The calculated HUMO and LUMO for 2-Au-InTeCl-Bulk at (a) 0.8 V, (b) 1.5 V.

of 1.67 eV for Li along the x-axis which is a bit smaller than that of InTeCl bilayer as shown in Fig. 19 (b) and significantly higher than the bulk as shown in Fig. 19 (c). The value of the energy barrier is an important property that determines the rate of a reaction or process. The understanding and controlling the energy barrier is critical for designing materials with desired properties. Here InTeCl bilayer offers more opposition during the diffusion of Li rather than the slab. This is possibly due to the higher probability of the interaction of Li with the host atoms in the bilayer in comparison to the monolayer.

The value of transition barrier for InTeCl bilayer along the y-axis is 1.7eV as shown in Fig. 19 (b) which is higher than the InTeCl slab and bulk periodicity. It points out that the bilayer offers the maximum opposition to the diffusion atom within the structure and hence slower the reaction. Fig. 19 (c) shows the diffusion pathway for the bulk InTeCl which is more suitable than the 2D InTeCl because it offers less energy barrier of 1.32 eV which is significantly lower than the slab and the bilayer. Hence, the diffusion rate is much higher and the reaction will be fast in comparison with the other two periodicities.

4. Summary

A detailed theoretical study was carried out to investigate the structural, electronic and transport properties of InTeCl in bulk and slab periodicities. The structural, dynamical and thermal stability of the materials were studied. The structures were optimized and lattice parameters were computed. The single-point calculations were performed to determine the electronic properties of materials. The NEGF technique was used to determine the ballistic transport properties of the nanodevices based on the InTeCl based materials. The IV characteristics and transmission spectra were determined to check electronic transmission through electrodes towards the scattering region. The Au-contacts appeared to play essential role in current-voltage behavior. It is found that an increase in the channel length affected the transport properties of InTeCl and it resulted in rectification characteristics which are determined using transmission spectra at various applied bias voltages and with the help of MPSH states. The diffusion pathways simulations were carried out using NEB which revealed that the bulk InTeCl offers the minimum transition barrier of 1.32 eV to the diffusing Li atoms. The reported findings will help designing the field-effect transistor nanodevices based on InTeCl.

Ethical approval

Not applicable.

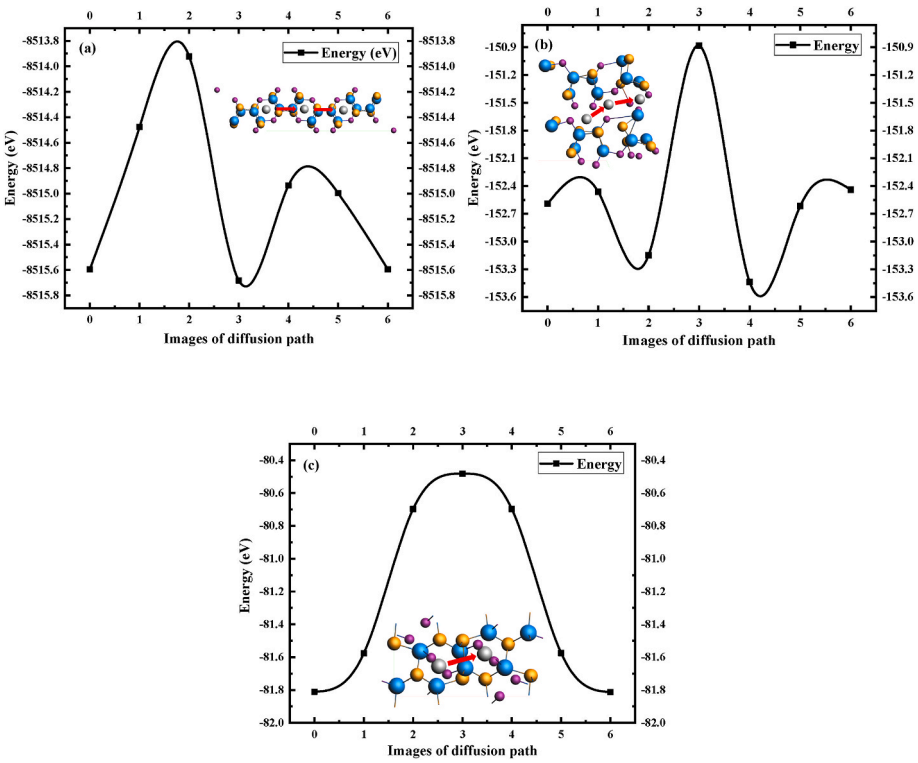

Fig. 19. The calculated Cl-NEB simulation for Li atom migration pathways in the host InTeCl (a) for slab periodicity along the x-axis with energy-barrier 1.67 eV (b) for bilayer along the y-axis with energy-barrier 1.70 eV (c) for bulk along the z-axis with energy-barrier 1.32 eV.

Funding

Not applicable.

Availability of data and materials

Not applicable.

CRediT authorship contribution statement

Hira Batool: Writing – original draft, Investigation, Data curation. **Abdul Majid:** Supervision, Resources, Methodology, Conceptualization. **Mohammad Alkhedher:** Writing – review & editing, Visualization, Validation. **Niyazi Bulut:** Writing – review & editing, Visualization, Validation. **Ibrahim Al-Adwan:** Writing – review & editing, Visualization, Validation.

Declaration of competing interest

The authors declare that they have no known competing financial interests or personal relationships that could have appeared to influence the work reported in this paper.

Data availability

Data will be made available on request.

References

[1] W.H. Guo, et al., Face-shared octahedral dimer In2O7S2 in the non-centrosymmetric barium indiumsilicate oxysulfide Ba2In2Si3O10S, Eur. J. Inorg. Chem. 2016 (12) (2016) 1846–1850.
[2] O.I. Siidra, et al., Lead oxychloride borates obtained under extreme conditions, Inorg. Chem. 55 (17) (2016) 9077–9084.
[3] J.-R. Xiao, et al., A review of the structural chemistry and physical properties of metal chalcogenide halides, Coord. Chem. Rev. 347 (2017) 23–47.
[4] J. Beck, New forms and functions of tellurium: from polycations to metal halide tellurides, Angew Chem. Int. Ed. Engl. 33 (2) (1994) 163–172.
[5] H.F. Franzen, W. Hönle, H.G.v. Schnering, Nb2Y2X6, a novel type of NbIV compounds with cross-linked Nb2 and Y2 dumbbells (Y= Se, Te; X= Br, I), Z. Anorg. Allg. Chem. 497 (2) (1983) 13–20.
[6] T.R. Halbert, 41244 Intercalation Chemistry of Metal Chalcogenohalides, Intercalation Chemistry, 2012, p. 375.
[7] H. Schäfer, F. Wartenpfuhl, Das chrom (III)-oxychloride CrOCl, Z. Anorg. Allg. Chem. 308 (1-6) (1961) 282–289.
[8] J. Beck, Über chalkogenidhalogenide des chroms synthese, kristallstruktur und magnetismus von chromsulfidbromid, CrSBr, Z. Anorg. Allg. Chem. 585 (1) (1990) 157–167.
[9] K. Ishizaka, et al., Giant Rashba-type spin splitting in bulk BiTeI, Nat. Mater. 10 (7) (2011) 521–526.
[10] M. Bahramy, et al., Emergence of non-centrosymmetric topological insulating phase in BiTeI under pressure, Nat. Commun. 3 (1) (2012) 679.
[11] M. Bahramy, et al., Emergent quantum confinement at topological insulator surfaces, Nat. Commun. 3 (1) (2012) 1159.
[12] D. VanGennep, et al., Evolution of the Fermi surface of BiTeCl with pressure, J. Phys. Condens. Matter 29 (29) (2017), 295702.
[13] Q.H. Wang, et al., Electronics and optoelectronics of two-dimensional transition metal dichalcogenides, Nat. Nanotechnol. 7 (11) (2012) 699–712.
[14] X. Wang, et al., Pressure-induced structural and electronic transitions in InTeI, Phys. Rev. B 104 (6) (2021), 064104.
[15] H. Qu, et al., Electronic structure and transport properties of 2D RhTeCl: a NEGF-DFT study, Nanoscale 11 (43) (2019) 20461–20466.
[16] W. Zhou, et al., DFT coupled with NEGF study of a promising two-dimensional channel material: black phosphorene-type GaTeCl, Nanoscale 10 (7) (2018) 3350–3355.
[17] Y. Zhou, et al., Pressure-induced superconductivity in a three-dimensional topological material ZrTe5, Proc. Natl. Acad. Sci. USA 113 (11) (2016) 2904–2909.
[18] A. Jain, et al., Commentary: the Materials Project: a materials genome approach to accelerating materials innovation, Apl. Mater. 1 (1) (2013), 011002.
[19] R. Kniep, et al., Phasenbeziehungen in Systemen In2X3– InY3 sowie Strukturbeziehungen, Kristallzucht und optische Absorption von Verbindungen InXY [X= Se, Te; Y= Cl, Br, I]/Phase Relations in Systems In2X3– InY3 and Structural Relations, Crystal Growth and Optical Absorption of Compounds InXY [X= Se, Te; Y= Cl, Br, I], Zeitschrift für Naturforschung, 2014.
[20] R. Kniep, et al., Phasenbeziehungen in Systemen In2X3– InY3 sowie Strukturbeziehungen, Kristallzucht und optische Absorption von Verbindungen InXY [X= Se, Te; Y= Cl, Br, I]/Phase Relations in Systems In2X3– InY3 and Structural Relations, Crystal Growth and Optical Absorption of Compounds InXY [X= Se, Te; Y= Cl, Br, I], Z. Naturforsch. B Chem. Sci. 36 (12) (1981) 1520–1525.
[21] S. Jiang, et al., InTeI: a novel wide-bandgap 2D material with desirable stability and highly anisotropic carrier mobility, Nanoscale 12 (10) (2020) 5888–5897.

[22] C. Fonseca Guerra, et al., Towards an order-N DFT method, Theor. Chem. Acc. 99 (1998) 391–403.
[23] A.D. Becke, Density-functional exchange-energy approximation with correct asymptotic behavior, Phys. Rev. 38 (6) (1988) 3098.
[24] E. van Lenthe, E.-J. Baerends, J.G. Snijders, Relativistic total energy using regular approximations, J. Chem. Phys. 101 (11) (1994) 9783–9792.
[25] E. Van Lenthe, A. Ehlers, E.-J. Baerends, Geometry optimizations in the zero order regular approximation for relativistic effects, J. Chem. Phys. 110 (18) (1999) 8943–8953.
[26] E.v. Lenthe, E.-J. Baerends, J.G. Snijders, Relativistic regular two-component Hamiltonians, J. Chem. Phys. 99 (6) (1993) 4597–4610.
[27] M. Arshad Javid, et al., Structural, electronic and optical properties of LiNbO3 using GGA-PBE and TB-mBJ functionals: a DFT study, Int. J. Mod. Phys. B 32 (14) (2018), 1850168.
[28] W. Li, et al., Density functional theory and beyond for band-gap screening: performance for transition-metal oxides and dichalcogenides, J. Chem. Theor. Comput. 9 (7) (2013) 2950–2958.
[29] S. Datta, The non-equilibrium Green's function (NEGF) formalism: an elementary introduction, in: Digest. International Electron Devices Meeting, IEEE, 2002.
[30] J.-S. Wang, et al., Nonequilibrium Green's function method for quantum thermal transport, Front. Phys. 9 (2014) 673–697.
[31] M. Ghorbani-Asl, Electronic Transport through Two-Dimensional Transition-Metal Chalcogenides, Jacobs University Bremen, 2014.
[32] S. Poncé, et al., First-principles calculations of charge carrier mobility and conductivity in bulk semiconductors and two-dimensional materials, Rep. Prog. Phys. 83 (3) (2020), 036501.
[33] X. Xie, et al., First-principles studies in Mg-based hydrogen storage Materials: a review, Energy 211 (2020), 118959.
[34] G. Henkelman, B.P. Uberuaga, H. Jónsson, A climbing image nudged elastic band method for finding saddle points and minimum energy paths, J. Chem. Phys. 113 (22) (2000) 9901–9904.
[35] N.E. Ofili, Adsorption of Actinides on Mineral Surfaces, The University of Manchester, 2021 (United Kingdom).
[36] K. Huang, Y. Liu, H. Liu, First-principles study of the adsorption and diffusion mechanisms of lithium dendrite growth, Mol. Simulat. (2022) 1–8.
[37] H. Hahn, W. Nickels, Zur Struktur der Chalkogenidhalogenide des Indiums, Z. Anorg. Allg. Chem. 314 (5-6) (1962) 307–320.
[38] R. Kniep, A. Wilms, Phase relations in the InBr3-In2Te3 system and the crystal structure of InTeBr, Mater. Res. Bull. 15 (6) (1980) 763–770.
[39] V. Safonov, et al., Indium-tellurium-chlorine system, Zh. Neorg. Khim. 22 (3) (1977).
[40] R. Kniep, et al., Phase relations in systems IN2X3-INY3 and structural relations, crystal growth and optical absorption of compounds inxy (X= SE, TE; Y= CL, BR, I), Chem. Inf. 13 (13) (1982) no-no.
[41] H. Zheng, et al., Monolayer II-VI semiconductors: a first-principles prediction, Phys. Rev. B 92 (11) (2015), 115307.
[42] S. Zhang, et al., Three-dimensional metallic boron nitride, J. Am. Chem. Soc. 135 (48) (2013) 18216–18221.
[43] A. Savin, et al., ELF: the electron localization function, Angew Chem. Int. Ed. Engl. 36 (17) (1997) 1808–1832.
[44] K. Ohwada, On the Pauling electronegativity scales—I, Polyhedron 2 (5) (1983) 423–424.
[45] M.A. Spackman, D. Jayatilaka, Hirshfeld surface analysis, CrystEngComm 11 (1) (2009) 19–32.
[46] B. Cordero, et al., Covalent radii revisited, Dalton Trans. (21) (2008) 2832–2838.
[47] R.D. Shannon, Revised effective ionic radii and systematic studies of interatomic distances in halides and chalcogenides, Acta Crystallogr. Sect. A Cryst. Phys. Diffr. Theor. Gen. Crystallogr. 32 (5) (1976) 751–767.
[48] A. Jalil, et al., 2D CoGeSe3 monolayer as a visible-light photocatalyst with high carrier mobility: theoretical prediction, Appl. Surf. Sci. 565 (2021), 150588.
[49] A.A. Emery, C. Wolverton, High-throughput DFT calculations of formation energy, stability and oxygen vacancy formation energy of ABO3 perovskites, Sci. Data 4 (1) (2017), 170153.
[50] S. Soni, et al., Understanding the role of parallel pathways via in-situ switching of quantum interference in molecular tunneling junctions, Angew. Chem. Int. Ed. 59 (34) (2020) 14308–14312.
[51] M. Syaputra, et al., Study on transport properties of silicene monolayer under external field using NEGF method, in: AIP Conference Proceedings., AIP Publishing LLC, 2015.
[52] S. Choudhary, S. Qureshi, Effect of radial and axial deformation on electron transport properties in a semiconducting Si-C nanotube, J. Nano Electron. Phys. 3 (1) (2011) 584.
[53] Y. Zhao, et al., Dithiocarbamate assembly on gold, J. Am. Chem. Soc. 127 (20) (2005) 7328–7329.
[54] B. Huang, et al., Length-dependent electronic transport properties of the ZnO nanorod, Micromachines 10 (1) (2018) 26.
[55] Q. Han, et al., Electrical transport study of single-walled ZnO nanotubes: a first-principles study of the length dependence, J. Phys. Chem. C 115 (8) (2011) 3447–3452.
[56] K. Odbadrakh, P. Pomorski, C. Roland, Ab initio band bending, metal-induced gap states, and Schottky barriers of a carbon and a boron nitride nanotube device, Phys. Rev. B 73 (23) (2006), 233402.
[57] K. Odbadrakh, P. Pomorski, C. Roland, Ab initio bandbending and Schottky barriers of a carbon nanotube and boron nitride device, in: APS March Meeting Abstracts, 2006.
[58] Z. Li, D.S. Kosov, Dithiocarbamate anchoring in molecular wire junctions: a first principles study, J. Phys. Chem. B 110 (20) (2006) 9893–9898.
[59] G. Nazin, X. Qiu, W. Ho, Visualization and spectroscopy of a metal-molecule-metal bridge, Science 302 (5642) (2003) 77–81.
[60] A. Sarmah, P. Hobza, Mechanical force-induced manipulation of electronic conductance in a spin-crossover complex: a simple approach to molecular electronics, Nanoscale Adv. 2 (7) (2020) 2907–2913.
[61] M.B. Nardelli, J.-L. Fattebert, J. Bernholc, O (N) real-space method for ab initio quantum transport calculations: application to carbon nanotube–metal contacts, Phys. Rev. B 64 (24) (2001), 245423.
[62] A. Calzolari, et al., Ab initio transport properties of nanostructures from maximally localized Wannier functions, Phys. Rev. B 69 (3) (2004), 035108.
[63] C. Caroli, et al., Direct calculation of the tunneling current, J. Phys. C Solid State Phys. 4 (8) (1971) 916.
[64] S. Datta, Quantum Transport: Atom to Transistor, Cambridge university press, 2005.
[65] P.N. Samanta, K.K. Das, Electron transport properties of zigzag single walled tin carbide nanotubes, Comput. Mater. Sci. 81 (2014) 326–331.
[66] L. Lin, et al., Adsorption of gas molecules on Co-doped SnO2 (110): first-principles investigation, J. Appl. Phys. 129 (24) (2021), 244504.